Separation and Purification Technology 397 (2026) 138002

Contents lists available at ScienceDirect

Separation and Purification Technology

journal homepage: www.elsevier.com/locate/seppur

A novel porous media CFD model of direct contact membrane distillation in hollow fiber modules☆

N. Cancilla, M. Ciofalo, A. Tamburini *, G. Micale

Dipartimento di Ingegneria, Università degli Studi di Palermo, Viale delle Scienze Ed. 6, 90128 Palermo, Italy

ARTICLE INFO

Editor Name: B. Van der Bruggen

Keywords:
Desalination
Computational fluid dynamics
Direct contact membrane distillation
Hollow fiber membrane
Porous media
Mass transfer
Heat transfer

ABSTRACT

A computational model was developed to predict the performance of hollow fiber Direct Contact Membrane Distillation (DCMD) modules. Feed and permeate are modelled as fluids flowing through two interpenetrating porous media; each fluid may indifferently fill either the lumen or the shell side compartment. In regard to hydrodynamics, on the shell side the Darcy permeabilities are derived from previous CFD work by the present authors, based on a unit-cell approach, for both axial and cross flow, while on the lumen side they are derived from the assumption of Poiseuille flow. In regard to heat transfer, on the shell side Nusselt numbers are computed from classic literature correlations for flow past tube banks, while on the lumen side a constant value representative of parallel flow in pipes is adopted. Bulk and wall temperatures and salt concentrations on each side are alternatively computed in an iterative way and are coupled by volumetric source/sink terms describing heat and mass transfer to the fluid flowing on the opposite side. The model predicts 3-D flow, temperature and salt concentration fields, along with overall performance parameters such as freshwater yield and recovery ratio, as functions of geometry and inlet flow rates and temperatures, requiring only the membrane permeance and thermal conductivity as empirical input. It was validated against two independent sets of experimental data for tap and brackish water presented in the literature for two laboratory-scale hollow fiber DCMD modules; predicted yields and their dependence on feed inlet temperature or flow rate agreed satisfactorily with experimental measurements.

1. Introduction

The most prominent desalination technology today is Reverse Osmosis (RO), due to its advantages over thermal processes, such as low energy consumption and operating costs, the ability to operate at low temperatures, high recovery rates, lower environmental impact, and strong versatility [1]. However, today the study of alternative desalination technologies, to be compared or integrated in hybrid system with reverse osmosis [2], is also of great interest. Among these, Membrane Distillation (MD) offers specific benefits, such as the possibility of recovering low-grade waste heat or being combined with renewable energy sources, like solar thermal or geothermal energy [3]. Although its high thermal energy consumption currently makes it less competitive than reverse osmosis, one of the main advantages of this technology is that the energy required for desalination is independent of the salt concentration in the feed. This makes MD a potentially attractive option for desalination of highly concentrated feeds, such as brine or bittern [4], although a performance degradation may occur when concentrations exceed 10 wt% [5].

The driving force in Membrane Distillation is the water vapor partial pressure difference established across a hydrophobic membrane [6]. It is worth noting that, in MD, transmembrane pressures cannot exceed the so-called Liquid Entry Pressure (LEP), beyond which the wetting phenomenon of the hydrophobic membrane begins and its selectivity drops drastically; for commercial membranes, LEP values typically ranges from ~1 to a few bars [7]. The membrane is inserted in a module between a hot saline feed channel and a cold permeate compartment which, depending on the technique used, can contain distilled water, vacuum or air. Different permeate management methods have led to different types of MD processes, the advantages and limitations of which can be found in specialized texts [8]. Among the different types of MD, Direct Contact Membrane Distillation (DCMD) is considered the simplest to build and operate [9,10].

Economic analyses suggest that the cost-effectiveness of DCMD strongly depends on module design and energy source. A counter-flow

☆ This article is part of a Special issue entitled: 'Innovative Materials' published in Separation and Purification Technology.

* Corresponding author.
E-mail address: alessandro.tamburini@unipa.it (A. Tamburini).

https://doi.org/10.1016/j.seppur.2026.138002
Received 20 February 2026; Received in revised form 5 April 2026; Accepted 14 April 2026
Available online 15 April 2026

Nomenclature

A_{ext}	External surface area of hollow fibers (m^2)
C	Salt concentration (mol m^{-3})
C_m	Volumetric membrane permeance ($m^3\ m^{-2}\ s^{-1}\ Pa^{-1} = m\ s^{-1}\ Pa^{-1}$)
c_p	Specific heat capacity (J $kg^{-1}\ K^{-1}$)
D	Salt diffusivity in water ($m^2\ s^{-1}$)
d	Characteristic fiber diameter, inner or outer according to compartment (m)
h	Heat transfer coefficient (W $m^{-2}\ K^{-1}$)
H_{fg}	Latent heat of vaporization (J kg^{-1})
J_{vap}	Water vapor volumetric flux ($m^3\ m^{-2}\ s^{-1} = m\ s^{-1}$)
K	Darcy hydraulic permeability, Eq. (2) (m^2)
k	Turbulent kinetic energy ($m^2\ s^{-2}$)
l_T	Thermal development length (m)
Nu	Nusselt number (−)
p	Pressure (Pa)
Pe	Péclet number, RePr (−)
Pr	Prandtl number, $c_p\mu/\lambda$ (−)
Q	Flow rate ($m^3\ s^{-1}$)
q''	Wall heat flux (W m^{-2})
Re	Reynolds number, Eq. (1) (−)
s	Generic direction (m)
$S_{M,x}$,$S_{M,y}$,$S_{M,z}$	Momentum source terms along x, y, z, Eq 7.a, 7.b and 7.c (Pa m^{-1})
S_T	Heat source / sink term, Eq. (12) (W m^{-3})
S_W	Mass source / sink term, Eq. (8) (kg $m^{-3}\ s^{-1}$)
T	Temperature (K)
$\mathbf{u}$	Local velocity vector (m s^{-1})
u_x, u_y, u_z	Cartesian velocity components (m s^{-1})
V	Volume of fluid in a module (m^3)
V_{tot}	Total internal volume of a module (m^3)
x,y	Cartesian coordinates in cross section orthogonal to the fibers (m)
z	Cartesian coordinate parallel to the fibers (m)

Greek symbols

ε	Porosity (fluid volume / total volume) (−)
λ	Thermal conductivity (W $m^{-1}\ K^{-1}$)
μ	Dynamic viscosity (Pa s)
ρ	Density (kg m^{-3})
ω	Turbulent eddy frequency (s^{-1})
$\lvert\nabla p\rvert$	Pressure gradient along flow direction (Pa m^{-1})

Subscripts

avg	Average over module volume
b	Bulk value (mass flow average)
cond	Conductive
f	Feed
i	Inner
in	Inlet
m	Membrane, transmembrane
max	Mean velocity in constricted section
o	Outer
p	Permeate
s	Referred to the generic *s* direction
t	Transverse (lying in a plane orthogonal to the fibers)
turb	Turbulent
vap	Vaporization
z	Referred to the *z* direction

Superscripts

(i)	Generic iteration
sat	Saturation

Average

$\langle\Phi\rangle$	Superficial average

Acronyms and abbreviations

DCMD	Direct Contact Membrane Distillation
FV	Finite Volume
LEP	Liquid Entry Pressure
MD	Membrane Distillation
URF	Under Relaxation Factor

cascade of modules in cross flow reduces temperature differentials and conductive heat losses, achieving up to 90% stage thermal efficiency and thus mitigating a major drawback of DCMD compared to vacuum MD [11]. With low-cost steam or waste heat, DCMD starts becoming competitive with reverse osmosis [12,13] and can significantly reduce brine disposal costs by concentrating waste up to 20% salinity [14].

Fig. 1 shows a schematic representation of the DCMD based desalination process.

The feed water (for example, seawater) is first pre-heated by a heat exchanger, recovering the residual heat from the permeate exiting the MD module which, in its turn, is cooled. The remaining heat is delivered by a heat source that can be low grade waste heat or renewable energy (e.g., solar, geothermal, etc.). Now, the hot saline feed enters the module where only the water vapor passes through the pores of the hydrophobic membrane. The water vapor condenses into the freshwater flowing in the permeate channel, which is then used to exchange heat with the entering feed. The cold permeate is in part recirculated to the module, while another part represents the produced distilled water (yield). On

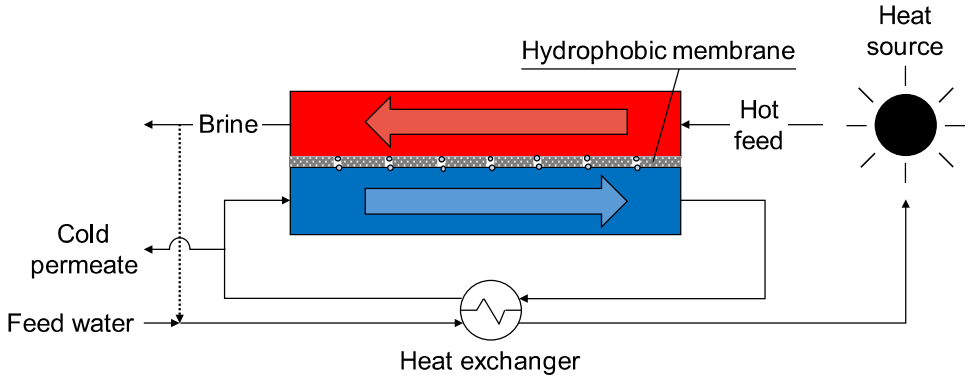

Fig. 1. Schematic representation of desalination in the Direct Contact Membrane Distillation process.

the feed side, the concentrated feed solution exiting the module (retentate) is now a brine, which can be discharged, or partially mixed and recycled with the feed stream.

The most common module configuration in DCMD is the spiral-wound one. However, in recent years, an increasing number of studies addressed Membrane Distillation considering the hollow fiber module configuration. For instance, Kariman et al. [15] predicted through simulations that the hollow fiber configuration exhibits higher flux and efficiency, as well as lower thermal energy consumption, compared to the flat sheet one, for any operational condition and membrane property investigated. In this geometry, which adopts the shell-and-tube heat exchanger design, a bundle of several thousands of hollow fibers is embedded in a shell. The size and number of fibers within the shell determine the bundle porosity (ratio of shell side fluid volume to total volume), which may strongly affect module performance [16]. The segregation between the lumen and shell side fluids is ensured by the presence of a sealing ("potting"), generally formed by curing an epoxy resin. The inlet and outlet of the feed and permeate streams in the module occur through appropriate ports.

The characteristics of the feed solution guides the choice of the lumen and shell side configuration. The *outside-in* flow, in which the feed flows on the shell side and the permeate on the lumen side, is the favorite option for feed subjected to crystallization phenomena or solution including suspended solids and foulants. As opposite, the *inside-out* flow, in which the hot feed flows on the lumen side, with no direct contact with the module wall, is preferred to reduce heat losses [17]. Both axial- and cross-flow orientations are common.

An extensive amount of both experimental and modelling research work on DCMD in hollow fiber membrane modules was conducted by Sirkar and co-workers. They started by experimenting rectangular cross flow modules for DCMD based desalination [18,19]. The modules had a membrane area in the range 0.011–0.025 m^2 and were later scaled up to ~0.28 m^2. They tested various feed compositions and diverse permeate flows configurations [20–22]. Pilot-scale tests [14] exhibited high water fluxes and stable membrane performances, with a water production rate of 2.35 L/min. Laboratory-scale modules, tested with de-oiled water from steam-flooded oil wells, showed that DCMD could recover 80% of water in a single step, without needing prior cooling or suffering from scaling issues [23], as opposite to reverse osmosis-based processes which required eight steps of treatments [24]. However, the rectangular module has limitations in scalability due to low packing density, high complexity in the assembly and significant dead volume. Despite good performance, this configuration leads to high fabrication costs, potential leakage, and scale-up challenges.

To address these issues, the same research group introduced a cylindrical cross flow module configuration with a surface area/volume of 1524 m^2/m^3, which is four times larger compared to that of the rectangular module [25]. This design increases packing density and reduces dead volume. Using the same type of fibers, the authors tested the cylindrical modules with salt feed solutions over a temperature range of 60–91 °C. They addressed also issues like membrane scaling and wetting. For example, in laboratory-scale tests with highly supersaturated brines they showed excellent resistance to scaling [26]. Even brines containing anti-scalants (like reverse osmosis retentates) did not cause membrane wetting, indicating strong operational robustness [27]. Recently, the same research group presented innovative fibers [28] and module design concepts [29], also adaptable to other MD configurations.

In the frame of the same research program, Sirkar and co-workers developed also a two-dimensional mathematical model, which was validated against experiments and used to optimize the module [25]. Several other models of MD based desalination modules containing hollow fiber membranes, often used to assess the influence of different parameters on module performance, have been reported in the literature [19,30]. In principle, the direct simulation of the entire ten thousand fiber bundle would be possible, but it would involve an unreasonable computational effort. To address this problem, the present authors simulated a unit cell of the bundle by means of CFD [31]. They studied the shell-side Nusselt number and hydraulic (Darcy) bundle permeability as functions of flow direction and Reynolds number in hollow fiber DCMD modules arranged both in regular lattices and random configurations, and derived useful hydrodynamics and heat transfer correlations [31]. As an alternative, some models by other authors use simulation approaches like the analytical cylindrical cell [32] or the 2-D porous media formulation [33]. In this latter approach, Marques Lisboa et al. [33] associated two porous media with the lumen and shell phases to study the influence of different membrane parameters (radius, thickness, thermal conductivity, mean pore diameter and porosity) on the energy efficiency of a DCMD hollow fiber membrane module. They modelled the bundle of hollow fibers using the Darcy anisotropic porous medium model and the convective-diffusive heat transfer equation in porous media in combination with the Dusty Gas model [8] for mass transport through the membrane.

The present study is aimed at developing a new model of two interpenetrating porous media for the simulation of fluid flow, heat and mass transfer in DCMD hollow fiber modules. To the best of the authors' knowledge, this is the first CFD three-dimensional porous media model for MD. It simultaneously accounts for:

- values of the Darcy hydraulic permeability derived from previously conducted unit cell small scale simulations, following a multiscale approach;
- transmembrane heat and mass fluxes, expressed as appropriate sink/source terms;
- the effects of fiber arrangement (regular or random), flow configuration (parallel-, cross- or mixed flow) and module geometry, described by changing simple modelling options.

As will be shown in the Results section, the use of a CFD-based model, albeit in the porous media approximation, proved to be highly effective in revealing aspects of the complex physical phenomena occurring in an MD module, and in highlighting weak design spots and suggesting potential improvements. Once properly validated, the present model can be employed to conduct parametric sensitivity analyses for assessing the influence of operating conditions, membrane properties and module design on the performance of a DCMD unit.

2. Models and methods

2.1. Main definitions and transport equations

In this work, for each of the two compartments (lumen side or shell side), the bundle porosity was defined as $\varepsilon = V/V_{tot}$, V being the volume of the relevant fluid and V_{tot} the total volume enclosed in the outer shell, including both fluids and fibers. The better to mimic available experiments, the feed fluid was assumed to flow in the shell side compartment and the permeate in the lumen side one, but the model can be applied, with minimal changes, also to the opposite configuration.

In the generic compartment (lumen side or shell side), the Reynolds number Re_s associated with a generic direction s was defined as:

$$\mathrm{Re}_s = \frac{\rho u_s \varepsilon d}{\mu} \tag{1}$$

Here, u_s is the component along s of the local velocity of the fluid in the compartment considered, ε is the compartment-specific porosity, while ρ and μ represent the fluid density and dynamic viscosity, respectively. The characteristic diameter d is the inner fiber diameter d_i for the lumen side compartment, and the outer fiber diameter d_o for the shell side compartment.

Note that the above definition makes the Reynolds number a local and direction-dependent quantity, thus allowing Darcy permeabilities, heat transfer coefficients or other flow-related quantities to be locally

expressed in the relevant porous medium as functions of the speed and direction of the flow. For practical reasons, among which the limitations of the computer code used, only two directions were considered, axial (along the fibers), denoted by the subscript z, and transverse (orthogonal to the fibers, i.e. lying in the cross-sectional xy plane), denoted by the subscript t. Of course, for the lumen side fluid the transverse velocity and Reynolds numbers were identically zero.

The Darcy hydraulic permeability along a generic direction, K_s, was defined as:

$$K_s = \frac{\mu\,\varepsilon u_s}{|\nabla p|_s} \tag{2}$$

where u_s is the local (in the porous media sense) velocity component along the s direction and $|\nabla p|_s$ is the pressure gradient along that direction. In particular, K_z denotes the permeability in the axial direction, while K_t represents the permeability in a generic transverse direction lying in the cross-sectional xy plane.

The fluid flow and the transport of enthalpy and salt are governed by the continuity, Navier-Stokes and transport equations to which appropriate source terms have been added to account for transmembrane fluxes and frictional resistances:

$$\nabla\cdot\mathbf{u} = S_W \tag{3}$$

$$\rho\mathbf{u}\cdot\nabla\mathbf{u} = -\nabla p + \mu\nabla^2\mathbf{u} + \mathbf{S}_M \tag{4}$$

$$\rho c_p\mathbf{u}\cdot\nabla T = \lambda\nabla^2 T + S_T \tag{5}$$

$$\mathbf{u}\cdot\nabla C = D\nabla^2 C \tag{6}$$

where $\mathbf{u}$ is the local velocity vector, p is the pressure, T is the temperature, c_p is the fluid specific heat capacity, λ is the fluid thermal conductivity, C is the salt concentration in water and D is its diffusion coefficient. Source terms S_W, S_M and S_T will be discussed in Section 2.3 below. Note that there is no source term in the salt concentration transport equation, Eq. (6), because there is no salt flux through the membrane (i.e., the retention of the membrane is 100%).

To avoid overcomplicating the notation, the above equations are written in a generalized form and apply to both fluids (feed and permeate). In the followings, a subscript "f" will be used to refer to the feed, while a subscript "p" will indicate the permeate.

2.2. Geometries simulated and computational domains

Figs. 2 and 3 show the computational domains simulated in this study, along with the corresponding module dimensions. Arrows indicate the flow directions of the hot feed water (red) and the cold permeate (blue). To facilitate a clearer understanding of the fiber arrangement in the two geometries, two-dimensional cross-sectional views of both configurations are schematically illustrated in the relevant insets.

Fig. 2 illustrates the rectangular cross flow geometry, representative of the "S/N 1006/1015" module used by Song et al. [14]. In this configuration, the hot feed water enters and exits the module on the shell side, flowing in the y direction orthogonal to the zx planes. The cold permeate flows along z on the lumen side of the hollow fibers.

In the experiments [14], the shell-side fluid (feed) entered and exited the module through inlet-outlet pipes and roughly perforated plates, each featuring a pattern of non-uniform hole sizes designed to approximate a uniform velocity profile. The lumen-side fluid (permeate) flowed into and out of the module through inlet-outlet chambers and finely perforated plates accommodating the hollow fibers. In the present model, these external components were not simulated; instead, both fluids were assumed to enter the rectangular domain with flat velocity profiles and to exit through boundaries defined by uniform, arbitrary pressure. These simplifications may influence the predicted overall flow distribution, with their impact diminishing as the perforated plates become more effective at producing a uniform flow distribution.

Fig. 3 displays the cylindrical cross flow geometry, representative of the "Large module III" as reported by Singh et al. [25]. For symmetry reasons, only one half of the computational domain was simulated, as shown in the graph, thereby reducing the computational load.

Only the "Dead-End mode" configuration was simulated, in which the hot feed water enters along $-z$ through the bore of the central feeder tube (CFT), flows radially outward through its completely permeable wall, crossing the fiber bundle, and exits via the four shell-side outlet ports. The opposite end of the central feeder tube is sealed. On the lumen side, the cold permeate flows through the fiber lumens along the longitudinal z axis direction (from left to right in Fig. 3).

In the experiments [25], the CFT consisted of a physical tube perforated with an unspecified number of holes of unknown diameter. In the present model, the tube wall was not explicitly simulated; instead, it was modelled as a surface with zero hydraulic and thermal resistance. For the lumen-side fluid (permeate), the same considerations apply as in the previous rectangular configuration, with the external chambers not explicitly simulated. Also in this case, these simplifications may influence the predicted overall flow distribution.

Table 1 summarizes the geometric characteristics of the computational domains for the two configurations adopted in the present simulations.

2.3. Computational model

The model simulates the Membrane Distillation process in hollow fiber membrane modules using the concept of two interpenetrating porous media. This approach has been previously employed by several researchers, including the authors of this work, to simulate membrane

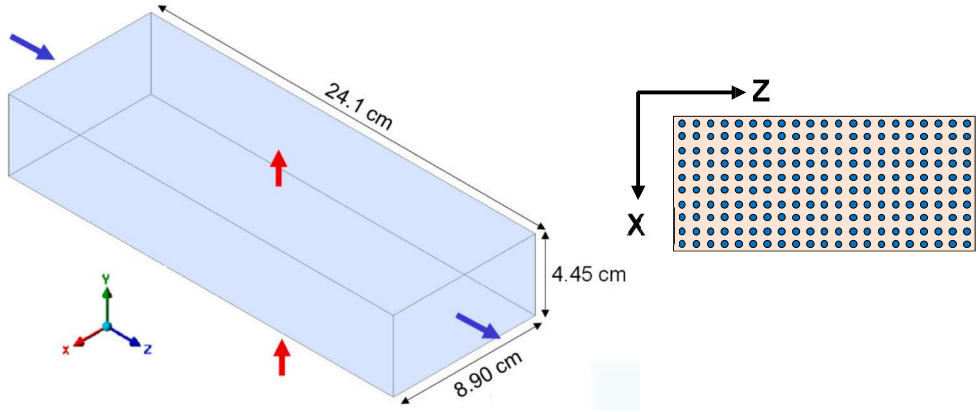

Fig. 2. 3–D computational domain for the rectangular cross flow geometry investigated by Song et al. [14].

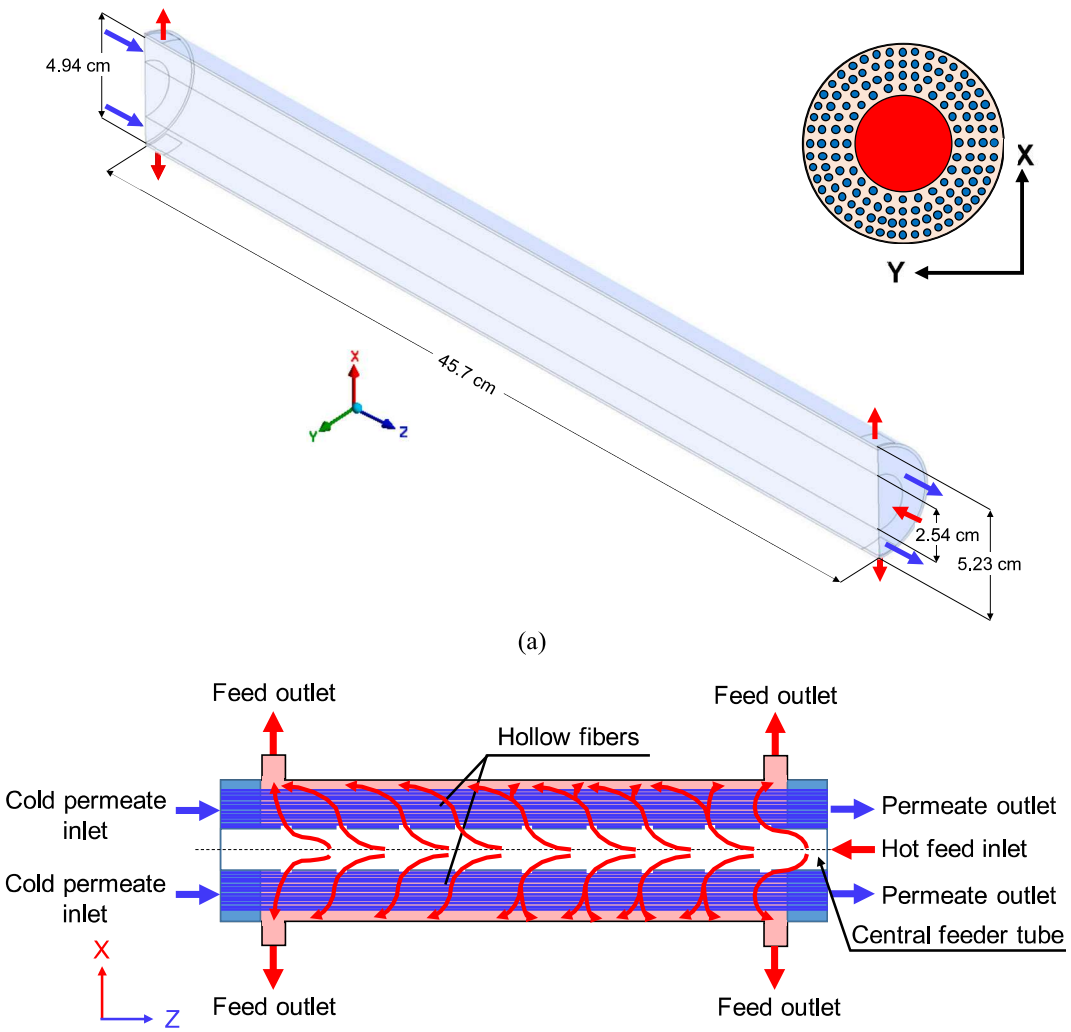

Fig. 3. Computational domain for the cylindrical cross flow geometry investigated by Singh et al. [25]. (a) 3-D axonometric view; (b) 2-D axial section showing hypothetical shell-side flow paths.

Table 1
Geometric characteristics of the two configurations investigated.

Geometry and name	Dimensions [m]	Number of fibers	Reference
Rectangular, "S/N 1006/ 1015"	width = 8.90×10^{-2} height = 4.45×10^{-2} length = 24.1×10^{-2} CFT diameter = 2.54×10^{-2} module diameter = 5.23×10^{-2}	2652	[14]
Cylindrical, "Large module III"	annular diameter of the porous region = 4.94×10^{-2} module length = 45.7×10^{-2}	1266	[25]

separation processes other than Membrane Distillation, such as hemodialysis [34,35], membrane bioreactors [36], and gas separation [37]. The feed and permeate are assumed to flow through two porous media representing the two compartments, occupying the same volume in space, but each characterized by a specific porosity value and specific Darcy permeability values (axial and transverse). As mentioned above, these permeability values were previously determined through unit-cell scale CFD simulations [16]. The characterization of the porous media can be incorporated into the CFD code used, which is Ansys CFX® 2023 R2 [38], by adding, consistently with Eq. (2), the following components of the momentum source term $\mathbf{S}_M$ to the right-hand side of the momentum equations, Eq. (4):

$$S_{M,x} = -\frac{\mu}{K_t}\varepsilon u_x \tag{7.a}$$

$$S_{M,y} = -\frac{\mu}{K_t}\varepsilon u_y \tag{7.b}$$

$$S_{M,z} = -\frac{\mu}{K_z}\varepsilon u_z \tag{7.c}$$

in which μ is the dynamic viscosity of the fluid considered, K_z and K_t are the axial and the transverse Darcy permeabilities for the same fluid, and u_x, u_y and u_z are the local velocity components along the x-, y- and z-directions, respectively.

On the lumen (permeate) side, the axial Darcy permeability K_z was calculated as $K_{z,p} = (1/32)\, d_i^2\, \varepsilon_p$ (corresponding to a friction coefficient of 64/Re). Note that this expression is not an approximation, but follows directly from the Hagen-Poiseuille theory for laminar, parallel flow in cylindrical ducts. In practical DCMD applications, the lumen-side flow is

typically laminar, and thus the above formulation of $K_{z,p}$ is appropriate. For instance, in the test cases simulated here, the lumen-side Reynolds number is ~266 for the rectangular geometry and ~140 for the cylindrical one. In regard to the transverse permeability $K_{t,p}$, since the lumen-side flow is confined within the fibers, it was set to zero in the simulations.

On the shell (feed) side, the values of the Darcy permeability K_z and K_t were determined by fully developed, steady state numerical simulations previously conducted by the authors [16] at unit cell scale. In these simulations, the computational domain consisted of a periodic unit of the fiber bundle containing one or a few fibers, with periodicity conditions applied to all variables across opposite boundaries.

For the rectangular configuration, which featured a shell side porosity of 0.791, the simulations yielded $K_{z,f} = 1.315 \times 10^{-1} d_o^2$ and $K_{t,f} = 6.50 \times 10^{-2} d_o^2$. For the cylindrical configuration, with a shell side porosity of 0.76, the corresponding values were $K_{z,f} = 1.023 \times 10^{-1} d_o^2$ and $K_{t,f} = 4.00 \times 10^{-2} d_o^2$. These values of K_z and K_t were subsequently incorporated into Eqs. (7).

2.3.1. Transmembrane mass transfer

Water vapor transfer through the porous membrane walls is simulated by adding the following mass source term to the right-hand side of the continuity equation, Eq. (3):

$$S_W = \pm J_{vap}\,\rho \frac{A_{ext}}{V_{tot}} \tag{8}$$

where ρ is the density, A_{ext} is the external surface area of the hollow fibers, J_{vap} is the water vapor volumetric flux through the membrane evaluated on A_{ext}, and V_{tot} is the total volume of the module. The "minus" sign applies to the feed and the "plus" sign to the permeate. In its turn, J_{vap} is calculated as:

$$J_{vap} = C_m\left(p_f^{sat} - p_p^{sat}\right) \tag{9}$$

in which C_m is the volumetric membrane permeance (expressed in m Pa^{-1} s^{-1}), while p_f^{sat} and p_p^{sat} are the saturation vapor pressures corresponding to the temperatures and salt concentrations on the feed and permeate sides of the membrane, respectively. Neglecting the minor influence of salt concentration, these values can be estimated using the Antoine equation, as has been done by many researchers [15,39–42]:

$$p^{sat} = \exp\left(23.238 - \frac{3841}{T - 45}\right) \tag{10}$$

with p^{sat} in Pa and T in K. The correction for salinity is less than 1% at the concentrations considered here (maximum feed concentration investigated 10,000 ppm).

2.3.2. Transmembrane heat transfer

Heat transfer through the membrane consists of two contributions: conduction across the membrane layer and its gas-filled pores (q''_{cond}) and latent heat associated with the water vapor (q''_{vap}). Therefore, the total feed to permeate transmembrane heat flux q''_m can be expressed as:

$$q''_m = q''_{cond} + q''_{vap} = \frac{(T_{f,m} - T_{p,m})}{\left(\frac{d_o/2}{\lambda_m}\right)\cdot\left(\ln\frac{d_o}{d_i}\right)} + \rho J_{vap} H_{fg} \tag{11}$$

where d_o and d_i are the outer and inner fiber diameters, respectively, λ_m is the thermal conductivity of the membrane, $T_{f,m}$ and $T_{p,m}$ are the temperatures at the membrane-feed and membrane-permeate interfaces, respectively, and H_{fg} is the latent heat of vaporization.

Similarly to the approach used for mass transfer, heat transfer through the membrane walls is simulated by adding the following thermal source term to the right-hand side of the energy transport equation, Eq. (5):

$$S_T = \pm q''_m \frac{A_{ext}}{V_{tot}} \tag{12}$$

where, once again, the "minus" sign applies to the feed side and the "plus" one to the permeate side.

2.3.3. Lumen-side heat transfer

In the present outside-in flow configuration, heat transfer through the permeate boundary layer occurs on the lumen side. The heat flux from the membrane-permeate interface to the bulk permeate q''_p is given by:

$$q''_p = h_p\left(T_{p,m} - T_{p,b}\right) \tag{13}$$

where $T_{p,b}$ is the bulk permeate temperature and h_p is the permeate (lumen) side heat transfer coefficient, computed as:

$$h_p = \mathrm{Nu}_p \frac{\lambda_p}{d_i} \tag{14}$$

λ_p being the thermal conductivity of the permeate water. For the lumen side Nusselt number, the value $\mathrm{Nu}_p = 4$ was assumed in all simulations. The rationale for this choice is that this value is intermediate between the theoretical solution in a circular tube for uniform wall heat flux (4.36) and that for uniform wall temperature (3.66), under fully developed, steady, laminar flow conditions [43]. The motivation for assuming laminar flow in the lumen has been discussed in Section 2.3. It is worth noting that small variations in the assumed value of Nu_p have a negligible effect on the transmembrane heat flux, since the thermal resistance on the lumen-side constitutes only a minor fraction of the overall fluid-to-fluid resistance.

In regard to the assumption of fully developed flow and heat transfer, it is well satisfied for the configurations considered here. The lumen-side Reynolds number is ~266 for the rectangular geometry and ~140 for the cylindrical one. The Prandtl number is $\mathrm{Pr} = \mu_p c_{p,p}/\lambda_p \approx 7$, and the lumen diameter is $d_i = 0.33$ mm in both cases. According to Graetz theory [43], the thermal development length is $l_T \approx 0.02\,\mathrm{RePr}\,d_i$, yielding values of ~11 mm and ~6 mm, respectively. These lengths represent only a small portion of the total fiber length in both geometries (241 mm and 457 mm, respectively).

The same conclusion applies *a fortiori* to the hydrodynamic development length, which depends on the Reynolds number rather than on the Péclet number (Pe = RePr) and thus is several times shorter than the thermal one. In any case, the values of $K_{z,p}$ and Nu_p could easily be modified to account for entry effects, should these become significant (e.g., at higher velocities or with larger fiber diameters).

2.3.4. Shell-side heat transfer

Conversely, heat transfer through the feed boundary layer takes place on the shell side. The heat flux from the bulk feed to the feed-membrane interface q''_f can be written as:

$$q''_f = h_f\left(T_{f,b} - T_{f,m}\right) \tag{15}$$

where $T_{f,b}$ is the bulk feed temperature and h_f is the feed (shell) side heat transfer coefficient, expressed as:

$$h_f = \mathrm{Nu}_f \frac{\lambda_f}{d_o} \tag{16}$$

λ_f being the thermal conductivity of the feed water. For the shell side Nusselt number Nu_f, since, in both the rectangular and cylindrical configurations, the feed encounters the fiber bundle in cross flow, the following experimental correlation proposed by Zukauskas [44] for staggered fiber arrays in cross flow was used:

$$\mathrm{Nu}_f = 1.04\,\mathrm{Re}_{f,max}^{0.4}\mathrm{Pr}_f^{0.36} \quad (\mathrm{Re}_{f,max} < 40) \tag{17.a}$$

$$Nu_f = 0.71\,Re_{f,max}^{0.5}Pr_f^{0.36} \quad (Re_{f,max} > 40) \tag{17.b}$$

in which $Re_{f,max}$ is the Reynolds number defined on the basis of the velocity u_{max}, which is the mean velocity in the narrowest section of the fiber array.

A major limitation of Eqs. (17) is the absence of a baseline value, leading to the prediction $Nu_f \to 0$ as $Re_{f,max} \to 0$. However, in the present study, the shell-side Reynolds numbers $Re_{f,max}$ exceed ~100 and ~14 (see Section 3) for the rectangular and cylindrical configurations, respectively. Therefore, the values of Nu_f predicted by Eq. (17.b) are not affected by this deficiency. While this issue is not relevant for the test cases considered here for model validation, it becomes unacceptable in a general-purpose model. In the absence of more reliable empirical correlations, it should be addressed by adopting alternative formulations, for example correlations derived from unit cell (single fiber) scale CFD simulations, as was done for the Darcy permeability.

In the cylindrical geometry, although laminar flow conditions prevail within the bundle, the central feeder tube through which the feed enters the module on the shell side has a diameter of 2.54 cm. As a result, the Reynolds number is high (Re ≈ 38,000, as will be discussed in Section 3.2) in that region, and the assumption of steady, laminar flow no longer holds. This makes it necessary to use a turbulence model. In the present simulations, the k-ω turbulence model was employed, as it is well suited for predicting fluid flows where laminar and turbulent regions coexist [45]. The k-ω model solves transport equations for the turbulent kinetic energy k and the turbulent eddy frequency ω. The turbulent eddy viscosity is then calculated as $\mu_{turb} = \rho k/\omega$.

In regard to shell-side entry effects, for cross flow the application of the Graetz theory is inappropriate. Literature results [43,44] are available only for larger Reynolds numbers or are in contradiction with our previous CFD results for developing flow [46]; however, they all indicate that entry effects are small and limited to a few rows of fibers. Therefore, in the present study it was decided to neglect entry effects also in cross flow (i.e., in the shell side), as in the model used by Song et al. [14] and Singh et al. [25]. If a reliable correlation were available, it could be easily incorporated into the model without introducing any significant computational burden.

2.3.5. General remarks on the porous media approach

It should be stressed that, in the porous media description of a fiber bundle, areal fluxes (i.e., mass, momentum and heat fluxes per unit area) are converted into equivalent volumetric source or sink terms. Similarly, quantities associated with the membrane wall, such as concentrations, shear stresses and temperatures, are no longer tied to a specific surface, but become distributed throughout the volume. At the module scale, however, this conversion does not affect the accuracy with which these quantities are evaluated. Conceptually, all quantities become volume averages performed over a certain number of fibers rather than strictly pointwise variables. Nevertheless, unlike in low-dimensional (1-D or 2-D) models, the large scale features of the flow, temperature and concentration fields are preserved, allowing their influence on overall module performance to be effectively investigated.

2.4. Membranes, modules and fluids properties

In this study, the hollow fiber membranes considered were those used by Song et al. [14] and Singh et al. [25]. These membranes are made of porous hydrophobic polypropylene, with an inner diameter d_i of 3.30×10^{-4} m, a wall thickness of 1.50×10^{-4} m, a maximum pore size of 0.6 μm, and a membrane porosity in the range of 0.6–0.8.

Table 2 reports the values of membrane permeance and conductivity provided in references [14,25], which were adopted in the present simulations.

The rectangular cross flow configuration ("S/N 1006/1015" module studied by Song et al. [14]), see Fig. 2, includes 2652 hollow fibers arranged in a staggered rectangular lattice, resulting in an internal membrane surface area of 0.6634 m^2 (external 1.267 m^2) and a bundle shell side porosity of 0.791. The cylindrical cross flow configuration ("Large module III – Dead End mode" studied by Singh et al. [25]), see Fig. 3, comprises 1266 hollow fibers approximately arranged in concentric circles around the central feeder tube, yielding an internal membrane surface area of 0.6 m^2 (external 1.145 m^2) and a bundle shell side porosity of 0.76.

Table 2
Properties of the polypropylene hydrophobic membrane considered in both investigated configurations.

Geometry	Membrane volumetric permeance C_m [m s^{-1} Pa^{-1}]	Membrane thermal conductivity λ_m [W m^{-1} K^{-1}]	Reference
Rectangular	4.17×10^{-10}	0.054	[14]
Cylindrical	9.17×10^{-10}	0.083	[25]

In regard to the thermophysical properties of salt water, assumed to be a simple NaCl solution in water, variations of density, dynamic viscosity, specific heat capacity, thermal conductivity, and latent heat of vaporization are accounted for as functions of both temperature and salt concentration. The correlations employed in this study are those selected by the present authors in reference [47], but are not reported here for the sake of brevity.

2.5. Boundary conditions

In both configurations, the inlet boundary conditions for both the feed and permeate were specified as imposed flow rates, while the outlet boundary conditions were set to an imposed pressure of zero (relative).

For the rectangular geometry, all remaining external surfaces were modelled as no slip wall(s) with zero mass flux. In regard to heat transfer, these surfaces were treated as adiabatic.

The cylindrical configuration presents a more complex scenario, as it includes both fluid domains (the permeate flowing through the central feeder tube and the annular region surrounding the bundle) and porous domains (the bundle of hollow fibers). The interfaces between the fluids and porous regions were handled using a "Domain Interface", with a "General Connection" model applied at the interface. The external cylindrical surface of the shell was defined as a no slip wall with zero heat and mass fluxes. The same conditions were applied to the closed end of the central feeder tube. A symmetry condition was imposed on all surfaces lying in the zx plane.

Table 3 summarizes inlet temperatures, salt concentrations and flow rates in the feed and permeate compartments for the two geometries investigated.

2.6. Computational grids

Prior to the final simulations, a grid-independence analysis was conducted to assess the sensitivity of the results to the level of discretization. Key quantities related to hydrodynamics, mass and heat transfer (e.g., the pressure drops in the feed and permeate compartments, and the water vapor and heat fluxes) were evaluated as functions of the number of finite volumes (FV). The inlet flow rates for the feed and permeate were set to 3.00×10^{-4} m^3 s^{-1} (18 L/min) and 4.17×10^{-5} m^3 s^{-1} (2.5 L/min), respectively, with values of inlet temperatures and concentrations as in Table 3.

For the cylindrical configuration, four computational grids were tested, characterized by a total number of FVs increasing from ~26,000 to ~820,000. A grid consisting of ~260,000 finite volumes showed a maximum discrepancy of less than 1% compared to the finest grid, confirming practical grid independence. Consistently, a grid with comparable resolution was also employed for the rectangular geometry. For a given geometry, the same grid was used for both the feed and permeate

Table 3
Temperatures, salt concentrations and flow rates imposed at the feed and permeate inlets.

Geometry	$T_{f,in}$ [K]	$C_{f,in}$ [mol m^{-3}]	$Q_{f,in}$ [m^3 s^{-1}]	$T_{p,in}$ [K]	$C_{p,in}$ [mol m^{-3}]	$Q_{p,in}$ [m^3 s^{-1}]
Rectangular	363.15	0.58	Variable	293.15	0	$1.67{\cdot}10^{-4}$
Cylindrical	Variable	171.8	$3.00{\cdot}10^{-4}$	297.15	0	$4.17{\cdot}10^{-5}$

simulations. In all cases, the computational grids consisted only of hexahedral volumes, which are known to provide more accurate results compared to tetrahedral or hybrid grids under comparable discretization level [48]. The main characteristics of the grids used in the final simulations are summarized in Table 4.

2.7. Simulation strategy

The simulation method involves an iterative procedure. In the model, feed and permeate are treated as two different fluids flowing through separate porous media, yet sharing the same module volume and exchanging both water and heat fluxes between them.

The procedure is schematically illustrated by the flowchart in Fig. 4 and is described in the following. Note that bulk and interface temperatures and concentrations are three-dimensional fields defined at each point of the computational domain. In the porous medium treatment, also fluxes of heat and water are space-dependent quantities defined at each point of the computational domain as volumetric source terms in the balance equations, and fluid-membrane interfaces are not explicitly simulated.

Preliminarily, the quantities common to both compartments (overall geometry and computational grid, membrane thermophysical properties) are set. Then the computational procedure proceeds by alternating, in an iterative fashion, simulations for the feed (shell side) and the permeate (lumen side) compartments.

The generic shell-side iteration, characterized by an odd index i, starts with the definition of compartment-specific input data (thermophysical properties of feed water, porous media characteristics, boundary conditions). Both the feed and permeate membrane interface temperatures ($T_{f,m}^{(i-1)}$ and $T_{p,m}^{(i-1)}$) are then read in from a file where they were stored at the end of the previous iteration. In the special case $i = 1$ (initialization), they are set equal to the bulk temperatures $T_{f,b}^{(0)}$ and $T_{p,b}^{(0)}$, which, in their turn, are assumed to be uniform and equal to the corresponding inlet values as listed in Table 3. Based on these previous temperatures, the saturation vapor pressures on the feed-membrane and permeate-membrane interfaces, $p_{f,m}^{sat}$ and $p_{p,m}^{sat}$, are computed using Antoine's formula, Eq. (10).

Subsequently, using the mass transfer expression in Eq. (9) and the appropriate value for the membrane permeance C_m, the water vapor flux $J_{vap}^{(i)}$ exiting the compartment simulated (feed) is calculated. This flux is then converted into a volumetric mass source term $S_W^{(i)}$ via Eq. (8) (formulated for the feed side, i.e., with a negative sign) as well as the total transmembrane heat flux $q_m^{(i)}$ using Eq. (11), in which the interface temperatures $T_{f,m}$ and $T_{p,m}$ are set to the "old" values $T_{f,m}^{(i-1)}$ and $T_{p,m}^{(i-1)}$.

The heat flux $q_m^{(i)}$ is then applied in two ways: first, it is converted into a volumetric thermal source term $S_T^{(i)}$ by using Eq. (12) (again with a negative sign); second, it is used to update the membrane-feed interface temperature for the current iteration, $T_{f,m}^{(i)}$, via the following equation:

Table 4
Key characteristics of the computational grids used for the investigated geometries.

Geometry	Total number of finite volumes	Number of finite volumes in the cross-sectional plane
Rectangular	206,064	1431
Cylindrical	262,016	2848

$$T_{f,m} = T_{f,b} + \frac{q_m^{''}}{h_f} \tag{18}$$

In Eq. (18), the bulk feed temperature, $T_{f,b}$, is computed by solving the energy transport equation, Eq. (5), while the feed side heat transfer coefficient h_f is obtained via Eq. (16) from the corresponding Nusselt number Nu_f, which, in its turn, is computed using the correlation given by Zukauskas (Eqs. 17). The computed distribution of $T_{f,m}$, obtained from this simulation, will likely differ from the previous distribution, thereby necessitating a new simulation on the feed side.

Before completing iteration i, key data are stored into a file to be used as input for the subsequent simulation (iteration i+1, performed on the permeate side). These stored values include the distributions of feed side Nusselt number, salt concentration on the feed side (computed in the current iteration via the scalar transport equation, Eq. (6)), and temperatures at the membrane-feed and membrane-permeate interfaces, $T_{f,m}^{(i)}$ and $T_{p,m}^{(i)}$.

To allow the convergence of the computational procedure, an under-relaxation factor (*URF*) is applied to the updated value of $T_{f,m}$. A typical value used is $URF = 0.2$. Since the current iteration solves only the feed side compartment, the temperature at the membrane-permeate interface $T_{p,m}$ is stored unchanged as computed in iteration i-1, in order to be passed to the subsequent permeate side iteration i+1.

The subsequent iteration (even iteration with index i+1) is on the permeate (lumen side) compartment. Once compartment-specific input data (thermophysical properties of permeate water, lumen-side porous media characteristics, boundary conditions) are defined, the simulation mirrors that described for iteration i.

Temperatures $T_{f,m}^{(i)}$ and $T_{p,m}^{(i)}$ are imported from the previously stored file and are used to calculate the saturation vapor pressures on the feed and permeate sides via Eq. (10). Using these pressures, the water vapor flux $J_{vap}^{(i+1)}$ is calculated through Eq. (9). This flux is then converted into a water vapor mass source term $S_W^{(i+1)}$ using Eq. (8) (formulated for the permeate side, i.e., with a positive sign).

The total transmembrane heat flux $q_m^{(i+1)}$ is then computed by using Eq. (11). This flux is then employed in Eq. (12) (with a positive sign) to compute the thermal source term $S_T^{(i+1)}$. Additionally, $q_m^{(i+1)}$ is used to update the membrane-permeate interface temperature for the current iteration (i+1), $T_{p,m}^{(i+1)}$, using the following equation:

$$T_{p,m} = T_{p,b} - \frac{q_m^{''}}{h_p} \tag{19}$$

Here, the bulk permeate temperature, $T_{p,b}$, is obtained by solving the energy transport equation, Eq. (5), this time applied to the permeate side compartment. The heat transfer coefficient on the permeate side h_p is computed via Eq. (14) with $Nu_p = 4$. As before, the newly computed temperature distribution $T_{p,m}^{(i+1)}$ is likely to differ from that computed in the previous iteration $T_{p,m}^{(i)}$, necessitating a new simulation on the permeate side to reach convergence.

Before completing iteration i+1, the following quantities are stored: the salt concentration distribution on the permeate side (obtained in the current iteration by solving Eq. (4)), and the temperatures $T_{p,m}^{(i+1)}$ and $T_{f,m}^{(i+1)}$. Note that in this case $T_{f,m}^{(i+1)}$ remains unchanged from $T_{f,m}^{(i)}$, as this iteration only solve the equations on the permeate side, while, as with the feed side simulation, an *URF* of 0.2 is typically applied to $T_{p,m}^{(i+1)}$ to aid convergence.

The primary parameter used to assess the convergence of the iterative procedure is the average water vapor mass flux, $\rho J_{vap,avg}$, computed

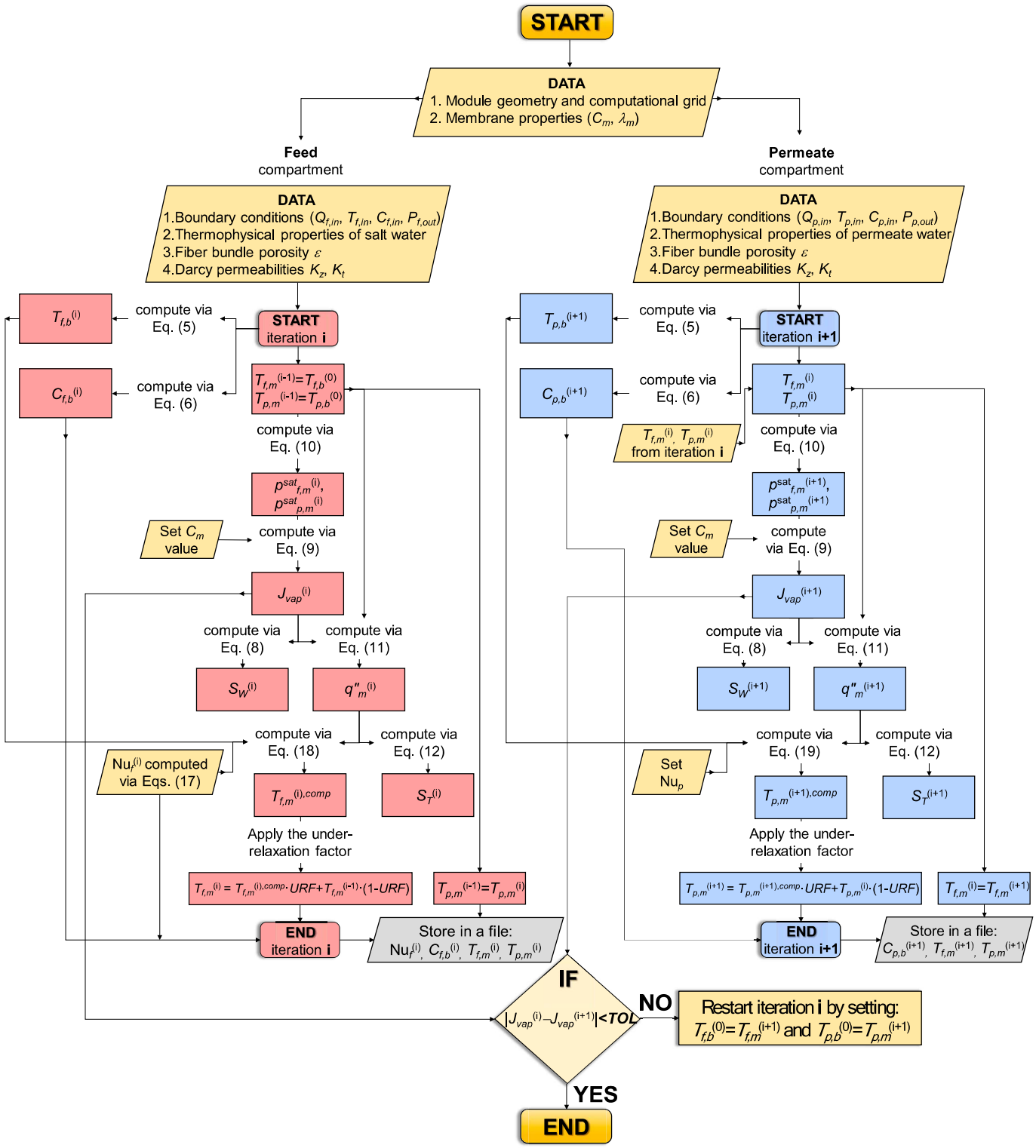

Fig. 4. Flow chart of the computational procedure.

as the volume averaged water vapor mass flux in the porous domain. Fig. 5 illustrates, as an example, the progression of the average water vapor mass flux as a function of the iteration index for a simulation case performed with the rectangular module geometry.

Notably, values of the average water vapor mass flux computed for the feed and permeate compartments (characterized by odd and even iteration indexes, respectively) lie on the same line and follow the same trend. The average water vapor flux decreases as the number of iterations increases, eventually reaching an almost constant value between the 24th and 25th iterations (in this case). Similar trends were observed in the simulations conducted for the other geometry investigated in this study. For the sake of brevity, the corresponding plots are not shown.